A MULTIPLE TIME-SCALE COMPUTATIONAL MODEL OF A TUMOR AND ITS MICRO ENVIRONMENT

CHRISTOPHER DUBOIS

University of California, Irvine, Dept. of Statistics
School of Information and Computer Science
3019 Bren Hall, Irvine, CA 92617-5100, USA

JESSE FARNHAM

Princeton University, Dept. of Computer Science
35 Olden Street, Princeton, NJ 08540-5233, USA

ERIC AARON

Wesleyan University, Dept. of Mathematics and Computer Science
265 Church St. Middletown, CT 06459, USA

AMI RADUNSKAYA

Pomona College, Dept. of Mathematics
610 N. College Ave., Claremont, CA 91711, USA

ABSTRACT. Experimental evidence suggests that a tumor's environment may be critical to designing successful therapeutic protocols: Modeling interactions between a tumor and its environment could improve our understanding of tumor growth and inform approaches to treatment. This paper describes an efficient, flexible, hybrid cellular automaton-based implementation of numerical solutions to multiple time-scale reaction-diffusion equations, applied to a model of tumor proliferation. The growth and maintenance of cells in our simulation depend on the rate of cellular energy (ATP) metabolized from nearby nutrients such as glucose and oxygen. Nutrient consumption rates are functions of local pH as well as local concentrations of oxygen and other fuels. The diffusion of these nutrients is modeled using a novel variation of random-walk techniques. Furthermore, we detail the effects of three boundary update rules on simulations, describing their effects on computational efficiency and biological realism. Qualitative and quantitative results from simulations provide insight on how tumor growth is affected by various environmental changes such as micro-vessel density or lower pH, both of high interest in current cancer research.

1. **Introduction.** Fast, biologically realistic hybrid cellular automaton-based tumor simulations could benefit cancer treatment by allowing researchers to simulate proposed treatment strategies in order to determine the most effective treatment. In thin, effectively two-dimensional slices of tissue, tumor development can be efficiently, realistically simulated using a *hybrid cellular automaton* (*HCA*), a grid

whose elements evolve based on a system of differential equations. This paper describes the development and implementation of an HCA-based mathematical model of tumor development that includes blood flow, nutrient diffusion, and cellular consumption of nutrients.

Time and space are both discretized in this HCA model; time passes in small, fixed-length steps, and each grid element corresponds to a small region of space, represented by local state data such as nutrient concentrations and cell populations. All grid elements are concurrently updated based on their local state and those of neighboring elements at the previous time step. That is,

$$S_{x,y}(t+1) = f(S_{x,y}(t), S_{x-1,y}(t), S_{x+1,y}(t), S_{x,y-1}(t), S_{x,y+1}(t)) \qquad (1)$$

where $S_{x,y}(t)$ is the state of element (x, y) at time t.

Cellular automata (CAs), originally described in [74], have a grid with infinite length in both dimensions; HCAs differ from CAs only in that some modeled quantities (e.g., nutrient concentrations) are continuously rather than discretely described, but the spatial representations of HCAs are based on grids exactly as fully discrete CAs are. In these CAs or CA-based models, all grid elements have the same number of neighbors, so they are all updated using the same set of rules. Practical implementations of CAs have finite grid sizes, however, so edge and corner elements have fewer neighbors than interior elements. Special *boundary rules* must therefore be devised to govern the updating of these elements. In this paper we discuss the implementation of a HCA model with three types of boundary rules.

2. **Background.** There is a long history of mathematical models of tumor growth that leads to this work. Early models consisted of systems of differential equations, such as [22], in which differential equations model effects of immune response to tumor growth, and [54], in which delays are introduced into the model. Previous models with differential equation-based representations of different cell populations, however, have ignored spatial characteristics such as blood vessel location and tissue heterogeneity. Furthermore, clinical insights can be gained from models that incorporate and integrate factors from a variety of biological systems that influence tumor development and treatment; models such as [3, 52], for example, incorporate elements ranging from angiogenic factors to cytotoxic immune cell dynamics and pH gradients. In particular, evidence suggests that local conditions such as nutrient availability, oxygen concentration, and local pH have key roles in carcinogenesis and tumor behavior, affecting tumor growth, malignancy, and response to treatment [72], and our model includes the effects of these factors on cell growth.

In this paper, we present a hybrid cellular automaton model of early solid tumor growth from an energy budget perspective, where nutrient consumption and ATP production are explicitly represented as dependent on oxygen concentration, available fuel concentration, and pH. The approach models tumor development over both time and space, and it incorporates the effects of variations in blood supply as well as the diffusion of oxygen and other nutrients on the morphology and aggressiveness of the tumor. Simulations of the model are compared with experimental data showing concentrations of hypoxic cells and tumor morphologies consistent with those observed in both *in vitro* and *in vivo* studies ([58], [38]).

Several approaches to the spatial modeling of tumors in the micro-environment have appeared in the literature. One approach uses partial differential equations and/or level-set methods to describe the evolution of the tumor boundary [11, 16]; others describe mechanical models of individual cells linked together [55], and others

bridge the gap between the continuum and discrete models, such as [59, 44, 57, 56] and [75]. Pertinent to the model presented in this paper is [10], which describes a mathematical model of the effect of cellular adhesion on tumor growth. Highly adhesive tumor cells are likely to result in a compact, circular tumor, whereas less adhesive cells may produce a more diffuse, branching tumor structure.

2.1. **CA models of tumor growth.** In [1], a cellular automaton-based model of tumor growth, the effects of differential blood flow and vessel adaptation are modeled. In this model, blood is treated as a non-Newtonian fluid which flows through a network of blood vessels. For example, red blood cells are distributed unevenly between the two daughter vessels in a network bifurcation; the daughter vessel with higher flow velocity receives a greater number of red blood cells. Furthermore, the blood vessel network adapts in order to best provide nutrients to the tissue. For example, a decrease in red blood cell flow rate may trigger an increase in blood vessel radius. Zero-flux boundary conditions are used in this simulation.

Another cellular automaton-based tumor simulation, described in [18, 45], includes the immune response. Two types of immune cells are modeled: natural killer (NK) cells and cytotoxic T lymphocytes (CTLs). NK cells wander the tissue area until encountering a tumor cell, which they then attack. When a tumor cell is lysed in this manner, additional CTLs are recruited to the same site, where they will attack other tumor cells in the immediate neighborhood. Immune cells in tumor-free locations die or randomly move to neighboring locations.

IMMSIM [53] is a cellular automaton-based simulation of immune system response. The IMMSIM model simulates discrete events such as the destruction of an individual antigen by an immune cell, rather than taking a continuous, differential equation-based approach. As in [1, 18, 45], biological components such as antigens and antibodies diffuse among grid elements. If two components are present in the same grid element, an interaction event such as antigen-antibody binding may occur. Each type of interaction has specific rules by which the probabilities of final outcomes are determined; the end result is then decided stochastically.

ParImm [4], a further development of IMMSIM, is another cellular automaton-based immune system simulator. Like IMMSIM, ParImm models cellular and molecular components of the immune system. In ParImm, cells are implemented as stochastic finite state machines, with states corresponding to possible cellular conditions, such as normal, resting, infected, or dead. Cellular interactions may result in a change in cellular state. For example, an interaction between an immune cell and an infected cell might might change the infected cell's state to "dead."

Several recent automata models allow cellular behavior to depend on local chemical concentrations. Dormann et al. reproduced the layered structure of avascular V-79 tumors using cellular automata governed by chemical signaling [24], while Patel incorporated H^+ ion production rates and randomly placed blood vessels to explore optimal micro-vessel densities and pH levels for tumor invasion [51]. In addition, Alarcon employed vascular dynamics in a cellular automaton model to explore the role of blood flow and oxygen distribution [1].

Smallbone et al. [63] use a hybrid cellular-automaton model to explore the interactions between the tumor and its environment, and the effect that these have on carcinogenesis and invasiveness. This model builds on these earlier models by incorporating the interdependency between tumor cell metabolism and local chemical concentrations. In particular, it takes into consideration the delivery of oxygen and other fuels via micro-vessels, the constriction of blood vessels due to pressure from

the surrounding cells, cell-cell adhesion, the synthesis of nutrients for the production of ATP, the budgeting of cellular energy towards growth and maintenance processes, and the production of acidic byproducts during glycolysis. In this model, cell proliferation and death is a deterministic function of available energy, in contrast to CA models in the literature which use probabilistic rules [27, 45, 18, 63].

Several non-biological cellular automaton-based simulation methods [31, 43, 30] also exist. While these simulations vary widely in their applications, all CA-based simulation methods require boundary rules. It is likely that the boundary rules discussed in this paper could be applied to other biological or non-biological grid-based methods.

2.2. **Tumor metabolism.** While tumor cells consume a variety of fuels including glutamine, palmitate, oleate and others, oxygen and glucose are the most significant contributors to cellular energy [33]. The model discussed by Patel et al. in [51] considers tumor metabolism as characteristically glycolytic, where cells rely on anaerobic pathways for the majority of ATP production, regardless of local oxygen availability. This concept of a glycolytic phenotype was first proposed in 1929 by Warburg after he found that mouse ascites cancer cells produced high amounts of lactate even with abundant oxygen available, evidence of aerobic glycolysis [76]. Currently, this concept underlies many approaches to basic cancer research as well as cancer prognosis and treatment.

However, recent experimental evidence challenges the perception of a glycolytic phenotype [76]. Guppy et al. [33] conclude that under aerobic conditions, the metabolism of MCF-7 tumor cells is not different from that of many normal cells. If tumor cells were characteristically glycolytic, they would rely on glucose for the majority of their ATP production, even with normal oxygen availability. On the other hand, because tumor cells often consume a markedly high rate of glucose, PET (positron emission tomography) has become a very popular technique for detecting and measuring a wide variety of tumors, supporting the concept of a glycolytic phenotype [49]. Gatenby and Gillies [29] have proposed a plausible Darwinian scenario in which the glycolytic phenotype evolves as a response to intermittent hypoxia in pre-malignant populations.

Some argue that the oxygen and glucose consumption rates associated with tumors are more likely due to a heightened "Pasteur effect," where low oxygen conditions force tumor cells to metabolize glucose less efficiently. In fact, the role of tumor oxygenation has received attention recently for a variety of reasons, especially after some researchers have found correlations between low oxygenation and metastatic progression [67], treatment resistance, and patient survival. Oxygen is delivered to tissue via an efficient network of microvasculature, but with increasing size, tumors often compromise blood flow which causes a decrease in oxygen perfusion, leading to hypoxic regions distributed heterogeneously within the tumor, [72],[46], [37], [23]. Our model extends previous work by simulating the progression of hypoxia, its influence on local cell metabolism, and the consequences for solid tumor growth. Our assumptions on the differences in cell metabolism between normal cells and tumor cells differ somewhat from those made in the model of Smallbone et al. [63], in that both tumor cells and normal cells can metabolize either aerobocially or glycolytically. This situation corresponds to what is described as the "second phase of growth" in the evolutionary scenario described in [63]. It supports the hypothesis set forth in [29] by showing that the cell metabolism is sensitive to very small changes in oxygen and hydrogen ion concentrations, and that a small number
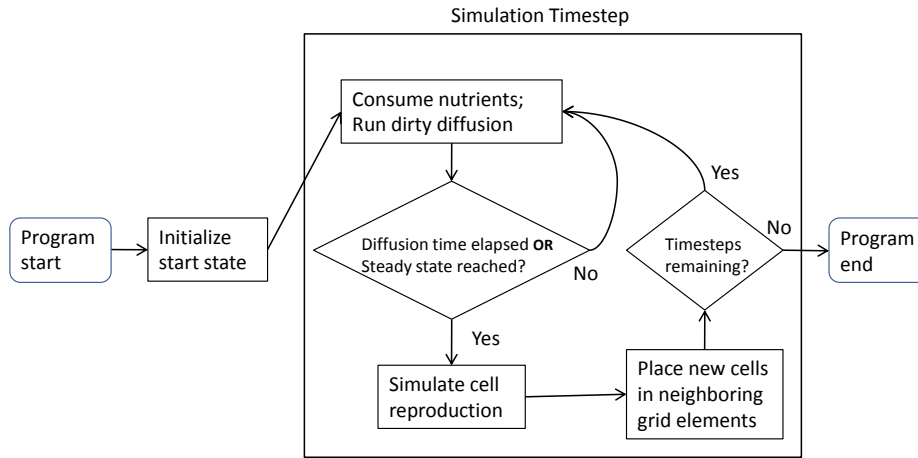
FIGURE 1. Diagram of the model flow during the implementation: the cell movement loop and the cell reproduction loop contain the inner diffusion loop.

of malignant cells can modify the micro-environment enough to allow the formation of a significant tumor mass.

3.   **Model development.** The simulation represents a thin, effectively two-dimensional slice of tissue with a cellular automaton data structure. Automaton grid elements represent small tissue areas and contain cell population and nutrient concentration data for those areas. To simulate the passage of time, all grid elements are updated in a two-step process: First, nutrient concentrations are updated by simulating diffusion and consumption by living cells. Second, cell populations are updated by simulating reproduction and death based on local nutrient concentrations in each grid element. In this implementation, cell growth, death and movement are determined by the amount of energy delivered via the blood vessels. This connects the "health" of the host directly to the growth of the tumor cells, and enables a connection between the macroscopic, holistic state of the larger organism with the local micro-environment of the tumor cells.

The diagram in Figure 1 indicates the model flow showing the inner diffusion loop inside the cell reproduction and movement loop. In this section we describe each of the modeling sub-steps in detail.

3.1.   **Model components: Nutrients, tissue and blood vessels.** The model uses a multi-layered $n \times n$ grid to describe cell populations and chemical concentrations throughout a two-dimensional simulation space. Each grid element represents a physical volume of 175x175x40 μm, or 10^{-6} ml. Thus the simulation space represents a thin layer of tissue 40 micrometers thick, a reasonable setting for studying the growth of some solid tumors, such as melanoma. Tumor cell and normal cell populations within each grid element are stored in $n \times n$ matrices, the matrix V_n represents normal cells; the tumor cell population is stored in two matrices, divided into V_t for viable cells, V_{nec} for necrotic cells. Thus, $V_n(i,j)$ gives the number of normal cells in the grid element representing the ith row and the jth column of the

discretized two-dimensional tissue. By modeling the way cell populations in each grid element interact with the local environment and neighboring cells, we are able to investigate early tumor growth in a qualitative and quantitative manner.

In vivo, blood vessels deliver nutrients (e.g., oxygen and other fuels) that cells consume, while these same cells produce waste (e.g., lactate) that is removed by the blood vessels. These two phenomena affect local extra-cellular chemical concentrations. Cell metabolism is dependent on the concentrations of nutrients and waste. In favorable conditions, cells can produce enough energy (ATP) from nearby nutrients to provide for cell maintenance and growth. In harsh conditions (e.g., in hypoxic regions), consumption rates are lowered and there is a significant decrease in doubling rate and an increase in cell death [14].

To simulate the micro-vascular network, a subset of grid elements are designated to contain blood vessels. Depending on the simulation desired, the distribution of blood vessels can be randomly generated, it can be prescribed according to some pattern, or it can be made to mimic an actual layer of tissue. In the case of a random distribution, the number of blood vessel elements is determined by experimental micro-vessel density values found in relevant literature, and might be one parameter of interest if the model is used to study the role of tumor angiogenesis, as was done in [51]. The size of the blood vessels can also be modified to be a portion of a grid element.

In a given simulation, all chemical concentrations generally begin at levels within normal ranges found in vivo. Small molecules will diffuse from the blood vessels at a rate dependent on the permeability of the vessel wall and on the gradient of chemical concentration. To store the local chemical concentrations within each grid element, three $n \times n$ matrices are used: the O matrix represents oxygen concentration $[O_2]$; G represents the concentration of glucose, representing the fuels available to the cells for maintenance and reproduction, and H represents the concentration of H^+ ions, determining the pH of the environment.

3.2. **Nutrient diffusion: "Dirty Diffusion".** The diffusion of oxygen, glucose and H^+ ions through the simulation space and the growth of cell populations are on two different time-scales: cell growth is on the order of days, but diffusion is on the order of seconds [51]. Thus, in our model, the diffusion process is modeled separately from cell proliferation, death and migration, allowing the simulation of processes on these two different time-scales. In this section, we describe the novel approximation methods used to speed up the simulation of the diffusion process, which occurs on the smaller time-scale and hence requires many more iterations than the cell-proliferation sub-routine.

Because small molecules diffuse on a time scale that is much faster than cell migration or proliferation, in many spatially dependent models of tumor growth that include the effects of nutrient concentration, the diffusion process is assumed to have reached its steady state so that the PDE can be replaced by an ODE. Alternatively, in a discretized version, the change in concentrations of nutrients is the solution of a large, sparse, system of linear equations (see Equation (5)). This system is then typically solved using an iterative method, such as the SOR method [51] or an LU decomposition [45]. In other implementations (e.g., [15]), the diffusion step is modeled explicitly using a finite element method or, as in [16], numerical solutions are obtained using level set methods. In all of these cases, computational costs are large: simulations on reasonably large grids can take hours unless some simplifying assumptions are made, such as radial symmetry [11, 39, 15].
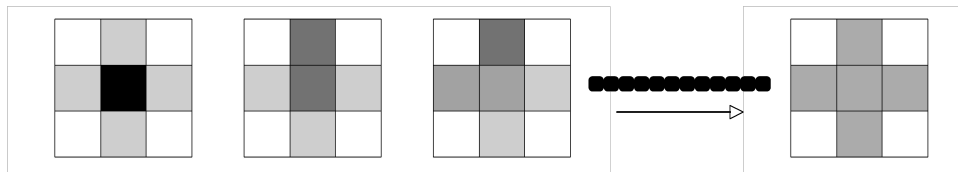
FIGURE 2. A graphical representation of the local averaging procedure that we call "Dirty Diffusion," used to simulate diffusion of small molecules. Rather than compute all of the steps shown in the figure, the algorithm immediately calculates the endpoint shown, i.e. the average of the 5 neighboring cells. The local averaging is done on 3×3 neighborhoods, where the 9 sets of neighborhoods are updated in a random order at each iteration in order to avoid the introduction of spurious drift.

In our method we exploit the difference in time scales without assuming a steady state for the diffusing nutrients by using a *local averaging* technique. Briefly, this technique involves averaging concentrations over 3×3 non-overlapping neighborhoods, known as *Margolus neighborhoods*, [26], and is depicted graphically in Figure 2. The idea is to by-step the intermediate graphs in this figure, and jump immediately from the first one to the last one. One interpretation of this numerical method is that in one step it gives the expected value of the concentrations of molecules moving randomly in space.

The center grid elements of each neighborhood are updated at each sub-iteration; therefore, 9 sub-iterations are required to update all grid elements. If the Margolus Neighborhoods are chosen in a random order, spurious drift patterns are avoided, and the numerical scheme converges very quickly to solutions of the continuous diffusion equation, Equation (3), without giving up the explicit time dependency. Experimentally measured diffusion coefficients (see Table A), are used to estimate the amount of time represented by the local averaging step, which will vary for each molecule.

We call our method "Dirty Diffusion," denoting a coarse approximation to the continuous representation of diffusion. A comparison of the Dirty Diffusion method and the SOR method is shown in Figure 3. This figure depicts solutions to an equation of the form given in Equation (3), where concentrations are constant at certain grid elements representing blood vessels (darkest grid elements), and the consumption function, k, is zero. On the sides of the grid, the algorithm is modified depending on which boundary condition is chosen. See Section 3.7 for details on these boundary rules.

Details of the Dirty Diffusion method. We explain the Dirty Diffusion method in more detail by describing its implementation for the solution of one diffusion equation. Consider a concentration of small molecules such as oxygen, denoted by $C(t, \mathbf{r})$, where t represents time and $\mathbf{r}$ represents the location in space. Suppose the molecules diffuse with constant diffusion coefficient, D, and are consumed by cells, represented by $T(\mathbf{r})$, at a rate $k(t, \mathbf{r}, T(\mathbf{r}))$. Then the partial differential equation describing the evolution of the concentration is:

$$\frac{\partial C(t, \mathbf{r})}{\partial t} = D \triangle C(t, \mathbf{r}) - k(t, \mathbf{r}, T(t, \mathbf{r})) \tag{2}$$
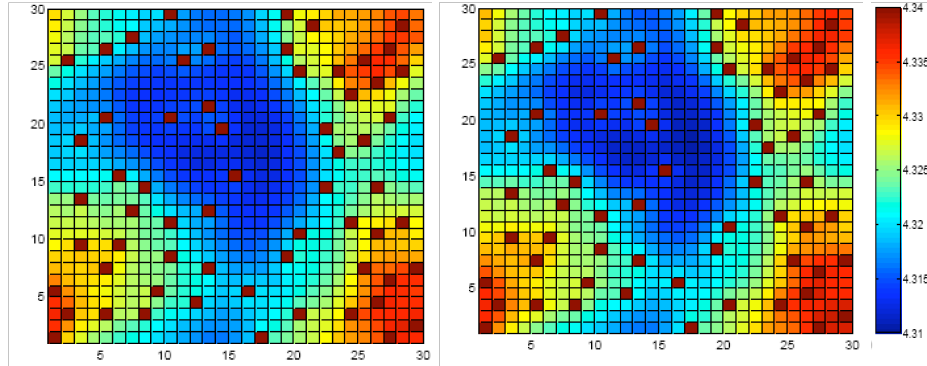
FIGURE 3. A comparison of the Dirty Diffusion method with the more traditional method of Successive Over-Relaxation (SOR). On a 30×30 grid with random blood vessels, the two methods produce results that agree closely. The SOR method (left) takes 21.453 seconds, while the Dirty Diffusion method (right) takes 6.672 seconds.

which in two dimensions becomes (we omit the independent variables where the dependence is clear):

$$\frac{\partial C}{\partial t} = D \left(\frac{\partial^2 C}{\partial x^2} + \frac{\partial^2 C}{\partial y^2} \right) - k(t, x, y, T(x, y)). \tag{3}$$

Discretizing space into an $n \times n$ grid, and discretizing time at intervals of size Δt gives the following discretized evolution rule for the concentration $C_{i,j}$ in the (i, j)th grid element:

$$C_{i,j}(t + \Delta t) \approx C_{i,j}(t) + \Delta t \frac{\partial C_{i,j}}{\partial t} \tag{4}$$

where the discretization of the partial derivative is:

$$\frac{\partial C_{i,j}}{\partial t} = D \frac{C_{i-1,j}(t) + C_{i+1,j}(t) + C_{i,j+1}(t) + C_{i,j-1}(t) - 4C(i, j)(t)}{(\Delta x)^2} - k_{i,j}(t, T_{i,j}(t))$$

and Δt is small relative to the diffusion rate, D. Note that the evolution rule depends on concentrations at the (i, j)th grid element and at the four neighboring elements. If the diffusion occurs at a much higher rate than consumption, then we might approximate the solution to Equation (3) by assuming that the nutrients first reach a steady state, and then are consumed. This is the approach taken by many modelers (e.g., in [51]). For the discretized equation, the steady state is a solution of n^2 equations of the form:

$$D \frac{C_{i-1,j} + C_{i+1,j} + C_{i,j+1} + C_{i,j-1} - 4C(i, j)}{(\Delta x)^2} = 0 \tag{5}$$

$$\therefore \quad C(i, j) = \frac{C_{i-1,j} + C_{i+1,j} + C_{i,j+1} + C_{i,j-1}}{4} \triangleq AVG4(i, j)$$

where $1 \leq i, j \leq n$. Thus, at the steady state of the diffusion portion of the equation, the concentration of nutrient in a given grid element is equal to the average of the concentrations in the four neighboring grid elements. We can therefore approach this steady state by successively replacing each grid element and its four neighbors

by their average value:

$$C_{i,j} \mapsto \frac{C_{i-1,j} + C_{i+1,j} + C_{i,j+1} + C_{i,j-1} + C_{i,j}}{5}. \tag{6}$$

The execution of one averaging step, Equation (6), simulates the diffusion of the molecules in and out of the neighboring cells over a time interval $\Delta \hat{t}$ which we can estimate as the expected time it takes for a molecule to diffuse across one grid element:

$$\Delta \hat{t} = \frac{(\Delta x)^2}{4D}. \tag{7}$$

If the rate of change of the cell population T is small relative to the rate of diffusion, then $T(x, y, t)$ can be approximated by a constant in the consumption term of Equation (3). Thus, after one time step of length $\Delta \hat{t}$, where the time step is short compared to the cell proliferation rate, we have the following update rule:

$$C_{i,j}(t + \Delta \hat{t}) = \frac{C_{i-1,j} + C_{i+1,j} + C_{i,j+1} + C_{i,j-1} + C_{i,j}}{5} - k_{i,j}(t, T_{i,j}(t))\Delta \hat{t}. \tag{8}$$

If Δt is the length of the proliferation time step, then in between each update of the cell matrices, Equation (8) is applied $\Delta t / \Delta \hat{t}$ times, or until an approximate steady state is reached, whichever comes first. See Figure 1 for a graphical representation of the program flow.

3.3. **Nutrient diffusion: Boundary values at blood vessels, modeling vascular constriction and collapse.** In our model, nutrients enter the tissue from simulated blood vessels and diffuse to locations with lower concentrations. Blood vessels are simulated by computing the *effective nutrient concentration* C_x at grid elements x that contain blood vessels, based on the *bloodstream nutrient concentration b* and *blood vessel permeability q*. The nutrient flux from a blood vessel to a neighboring grid element y is defined as $q(b - C_y)$, where C_y is the nutrient concentration in element y. This expression is then combined with Equation (6) to produce the following formula for C_x:

$$C_x = AVG4(x) + 5q(b - AVG4(x)) \tag{9}$$

For every element x that contains a blood vessel, the nutrient concentration in x is set to C_x. The rule given by Equation (8) is then applied, causing nutrients to diffuse away from blood vessels into the tissue, or causing metabolic by-products to diffuse from the tissue into the vessel. Modifications can be made if the grid element is not entirely filled with blood vessel, the details of which are omitted here.

We have developed Equation (8) which we use in the model to describe the diffusion and consumption/products of two nutrients and metabolic by-products. An important consideration in tumor growth is the collapse of vasculature inside the tumor due to constriction from the pressure of surrounding cells. This vascular collapse leads to two phenomena: angiogenesis [68, 35] and metastasis due to hypoxic stress [12, 8, 42].

Constriction is modeled by setting the blood vessel permeability q as a function of t, the total number of tumor cells in the five-element neighborhood surrounding the vessel. The formula and a graph is given in Figure 4

Figure 5 shows the constriction of blood vessels in the region occupied by tumor cells.
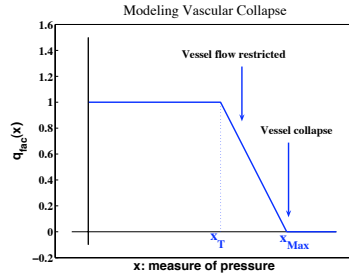
$$q(t) = \begin{cases} 1 & t \in [0, t_T] \\ 1 - \dfrac{t - t_T}{t_{Max} - t_T} & t \in [t_T, t_{Max}] \end{cases} \tag{10}$$

FIGURE 4. Blood vessel permeability, $q(t)$, as a function of t_T, the cell population at which vessel constriction begins, and t_{max}, the population at which the vessel collapses and blood flow is completely cut off.

3.4. **Nutrient consumption model.** Two types of nutrient molecules are explicitly modeled: oxygen and glucose. Metabolic waste is also modeled as free hydrogen ions created in the production of lactic acid. In the literature, cell metabolism and growth rates for EMT6/Ro tumor cells have been determined to be functions of local environmental factors such as glucose concentrations, oxygen availability, and pH [14]. Based on this experimental evidence, our nutrient consumption model has the following properties:

- Glucose consumption increases with glucose concentration.
- Oxygen consumption increases with oxygen concentration.
- Up to a saturation threshold, glucose consumption increases as oxygen concentration decreases.
- Oxygen consumption decreases as proton concentration increases.

This model is biologically motivated by two chemical processes used by cells to obtain energy: aerobic respiration and anaerobic respiration. Biological evidence for the model is presented in [14].

Recall that O denotes the current oxygen concentration (mM), G the current glucose concentration (mM), and H is the current ion concentration (mM), so that pH =-log10(H/1000). Casciari et al. [14] derived the following empirical equations for the rate of consumption of oxygen and glucose per cell (units are mol cell^{-1} s^{-1}). We have discretized and modified slightly the original equations from Casciari's paper to give the following equations describing the oxygen and glucose consumed by one cell in a time Δt.

$$\Delta O = \left(a_O + \frac{b_O}{GH^n} \right) \left(\frac{O}{O + k_O} \right) \Delta t \tag{11}$$

$$\Delta G = \left(a_G + \frac{c_\nu b_G}{O + \gamma} \right) \left(\frac{G}{G + k_G} \right) \left(\frac{1}{H^m} \right) \Delta t \tag{12}$$

where

$$\gamma = \frac{c_\nu b_G}{q_\nu H^m - a_G}. \tag{13}$$

The lower case letters are empirically determined constants whose values are listed in Table A. Based on experimental evidence [61, 41], our model assumes that normal cells consume less glucose than tumor cells as oxygen levels decrease. Therefore,
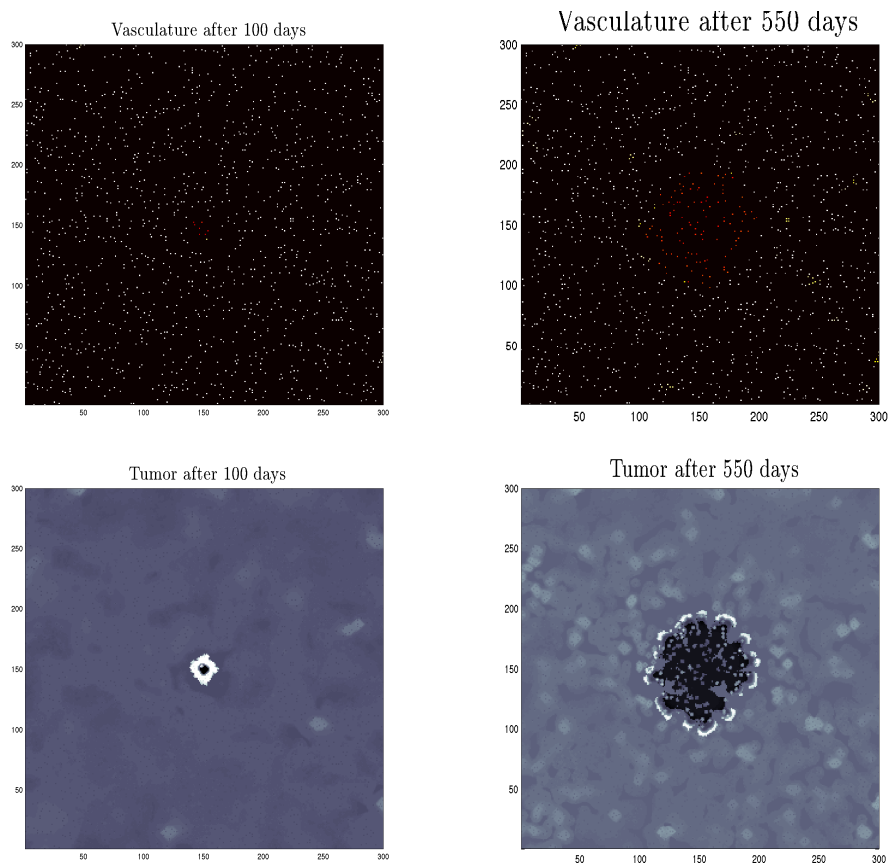
FIGURE 5. Simulations representing 100 days (leftmost panels) and 550 days (rightmost panels). Blood vessels are depicted in the top row: white dots represent unoccluded blood vessels, while colored dots are vessels that are restricted due to pressure from surrounding cells. The bottom row shows the cell levels at the same time points: viable tumor cells are shown in white, necrotic cells in black and normal cells in gray.

we introduce a parameter c_ν into the first term of Equation (12) to model the cell-specific sensitivity of dG/dt to O_2, where the subscript, ν, indicates the type of cell: normal cell, proliferating tumor cell, or necrotic tumor cell. The model also allows the maximum consumption rate, q, in Equation (13) to depend on cell type, again indicated by the subscript, ν. We have also modified the glucose consumption equation given in [14] under the assumption that the rate saturates as oxygen concentrations go to zero i.e. $-dG/dt$ can never exceed a fixed constant, q_ν. Assuming that the initial value of G is non-zero, the inclusion of a saturation term in Equation (12) insures that glucose levels will never reach zero. Therefore, we accept the empirically derived Equation (11) as it is given in [13], without adding a saturation term.

Metabolic Byproducts and pH: Derivation of Equation (14). Low extra-cellular pH is a trademark of solid tumor growth. When glucose is metabolized, cells produce lactic acid as a byproduct, which lowers the pH within the tumor (although other contributing factors have been suggested as well [36]). The blood vessels regulate pH by removing acidic byproducts, but in solid tumors this phenomena is inhibited by a chaotic vasculature [60]. Other buffers also aid in maintaining a pH suitable for normal tissue. Guppy et al. [33] estimate that the ratio of lactate to glucose production is 1.56 [1]. Accounting for buffering mechanisms, we estimate that only a small portion (10^{-5}) of the lactate molecules contribute to making the local environment more acidic. This estimate is the result of calibration of the model simulations to realistic values of tissue pH. Thus the change in [H^+] (mM) for a particular grid element is given by

$$\Delta H = (10^{-5})(1.56)\Delta G \tag{14}$$

We note here that other approaches to the mathematical modeling of ATP production have been taken that involve the modeling of the metabolic reactions themselves, rather than starting with the empirically derived rates of consumption as we do here. See [73, 6, 7] for examples of this approach in models of tumor spheroids. We feel that our simpler approach is suitable in this context, since we are interested ultimately in the long-term macroscopic features of tumor growth, vascular constriction and invasion, and one of our goals is computational efficiency.

The empirical constants, represented by lower case letters in Equations (11), (12) and (13), were determined experimentally by Casciari et al. [14]. Specific values are given in appendix A.

3.5. **Model of cell division and death.** The cell's ability to withstand a harsh environment plays a large role in tumor progression and resistance to treatment. However, experimental evidence shows that different cell lines, when exposed to hypoxic conditions, vary in their ability to withstand energy deprivation rather than vary in anaerobic consumption rates [62]. Thus, it is important to incorporate energy concepts into our model where cells experience energy deprivation in regions of low O_2 and low pH while cells are able to undergo mitosis in more favorable conditions.

We use a generalized framework for cellular energy budgeting formulated by Kooijman [40] that has been applied to tumor-host energy interactions [71]. This approach uses three key assumptions:

1. Each cell requires a certain rate of energy uptake in order to maintain itself, prioritizing energy use for common cell functions. Let M denote this per-cell maintenance cost.
2. There is also a fixed energy cost for mitosis, implying that the growth rate of a cell population is proportional to the energy available for growth. Let g denote the per-cell cost of mitosis.
3. The maintenance and mitosis parameters, M and g, respectively, depend on cell type.

---

[1]While the value of lactate production per glucose consumed, taken from [33], was obtained from experiments using a specific cell line (MCF-7 breast cancer cells), we use it here in the absence of other specific data. We point out that the lactate production could also be estimated from the amount of glucose and oxygen consumed: $\Delta H \approx 2(\Delta G - 1/6\Delta O)10^{-5}$, by counting how many glucose molecules are metabolized anaerobically, as long as this value is positive.

Thus, if $A(t)$ is the rate of energy intake (mol. (grid element)$^{-1}$ cycle^{-1}), the growth rate for a given number of cells V at grid element (i, j) is

$$\frac{dV_{ij}}{dt} = \frac{A_{ij}(t) - MV_{ij}}{g} \tag{15}$$

where, in general, the energy required for maintenance and mitosis will depend on cell type. Thus, in what follows, we add a subscript to the parameters M and g to denote their dependence on cell type.

Cells use ATP as a carrier of cellular energy storage, assembling ATP during metabolic processes and utilizing ATP for numerous cellular functions. Thus the energy intake rate, $A(t)$, described above corresponds to ATP availability rates. If we assume that all of the available energy is used, cell growth and death can then be determined from Equation (15) by calculating the available ATP. To calculate the amount of ATP energy derived from nutrient consumption, we consider oxidative and glycolytic metabolism separately. First, we consider the aerobic synthesis of ATP. We can calculate the total oxidative ATP turnover from the rate of oxygen consumption and a P:O ratio of 2.36 [33]. We may also calculate the number of glucose molecules utilized in oxidative processes, G_O, since the oxidization of one glucose molecule requires 6 molecules of O_2. Once the amount of glucose metabolized aerobically has been calculated, we may deduce that the rest of the glucose was metabolized anaerobically. Glycolysis is a far more inefficient process, producing at most 2 ATP per glucose molecule. In the model, we assume that, on average, 4 ATP molecules are produced for every 3 glucose molecules consumed anaerobically, taking into account any metabolic inefficiencies that may be present [48]. Note that this is a conservative estimate, and this aspect of the model could be adjusted to mimic particular environments. See, for example, the discussion in [7] where it is assumed that 2 ATP are produced per glucose molecule. Letting ATP_O and ATP_G denote the number of available ATP molecules produced aerobically and anaerobically, respectively, we have the following equations:

$$\Delta ATP_O = 2\Delta O \times 2.36 \tag{16}$$

$$\Delta ATP_G = \frac{4}{3}(\Delta G - \Delta G_O) = \frac{4}{3}\left(\Delta G - \frac{\Delta O}{6}\right) \tag{17}$$

Note that the last equation is only valid when $\Delta G \geq \Delta G_O$, i.e., if some anaerobic glycolysis occurs; otherwise $\Delta ATP_G = 0$. Thus, when enough oxygen is present, there may be no ATP molecules produced anaerobically. In experiments such as those reported in [14], it is possible that other fuel substrates are present. Therefore, while Equations (11) – (13) might violate the constraint $6\Delta G > \Delta O$, this would correspond to the presence of other fuel substrates in the experimental set-up. In our model, however, we assume that the only nutrients present are glucose and lactate. A refinement of the present model might take other fuels into account.

The total available ATP is the sum of Equations (16) and (17), which can then be used to calculate the change in the number of cells of type ν in grid element (i, j):

$$\Delta V_{i,j}^{\nu}(t) = \frac{\Delta ATP_{i,j}(t) - M^{\nu} V_{i,j}^{\nu}(t)}{g^{\nu}} \tag{18}$$

We remark that the calculation of the ATP produced as a function of the nutrient consumption rates provides insight on the energy status of our simulated cell populations. The total amount of energy available to the host at any given time might,

in principle, be a measure of the health of the organism, and could potentially be used for prognosis and/or treatment design.

See Appendix A for the values of the constants in all equations.

3.6. **Model of cell movement.** Each grid element represents a fixed spatial volume, so it can be filled with proliferating tumor cells, which can then invade neighboring grid elements. . However, cellular adhesion molecules, such as integrins and Tissue Factor (TF), play a large role in the mobility of tumor cells, affecting their interactions with neighboring cells and the surrounding extracellular matrix (ECM) [47]. When modeling the progression of a tumor through its different stages, it is necessary to consider the effects of cellular adhesion between cells and the ECM since the secretion or suppression of adhesion molecules is a possible mechanism for the onset of metastasis [2, 34, 28]. Mathematical models incorporating adhesion include [10] and [25], while [66] and [65] explore the relationship between cell-cell adhesion, pattern formation and disease prognosis.

Turner [70, 69], provides a method for estimating the diffusion coefficient for biological cells modeled as adhesive, deformable spheres by considering the "potential energy of interaction" between individual cells. Turner shows that the diffusion coefficient is proportional to the second derivative of the cells' energy density, $E(n)$,which can be derived in terms of the biological parameters of individual cells (such as elasticity and adhesiveness). This provides a way to consider a population of discrete cells macroscopically. A polynomial of Laundau-Ginzburg form:

$$E(n) = \frac{An^2}{2} + \frac{Bn^4}{4}$$

fits the solution of $E(n)$ quite well near the equilibrium density, where n is the density of cells, $A < 0$ and $B > 0$. We modify Turner's formula for $E(n)$ by setting it to zero below a minimum cell density, at which point adhesive forces have no effect, (see Figure 6).

Thus, below a specific minimal density (cells per grid element) $n_{\min}$, cells are assumed to make no physical contact, so E is zero. At densities greater than $n_{\min}$, cells begin to make contact and adhere, and E decreases to its minimum at the optimal cell density n_{eq}. Above n_{eq}, cell elasticity becomes more pronounced than adhesion, and E increases up to maximum possible density n_{max}.

In our simulations, each new tumor cell is placed in its grid element of origin, or in one of the four neighboring elements, according to the following rules. Tumor cells are placed first in grid elements with populations less than n_{eq}, with densely populated elements receiving cells before sparsely populated elements, in order to minimize total E over the local neighborhood. Once all elements in the five-element neighborhood containing the element of origin and the four adjacent elements are filled to n_{eq}, the remaining cells are distributed randomly over the neighborhood until $n_{\max}$ is reached in all grid elements. Any remaining new tumor cells are discarded due to overcrowding.

Adhesion between normal cells is assumed to be negligible compared with that of tumor cells, so no potential energy function is used for the distribution of normal cells. Newly generated normal cells are distributed randomly among the five-element neighborhood surrounding the grid element of origin.

3.7. **Boundary update rules.** For both nutrient diffusion and cell mobility, the conditions governing updates on the boundaries of CA grid elements are critical to the simulation, ensuring that proper biological context is represented. We have

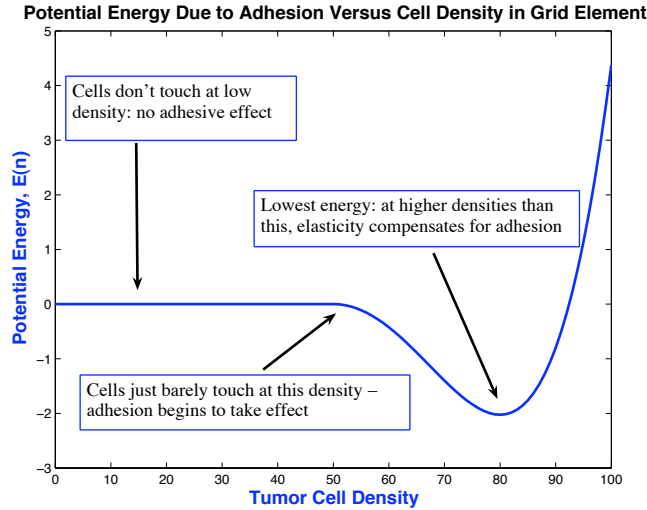**Potential Energy Due to Adhesion Versus Cell Density in Grid Element**

FIGURE 6. The potential energy of cell configurations is used to determine cell movement. Densities are given in cells per grid element. The potential energy function is zero for densities less than $n_{\min}$, at which density the cells are assumed to be "just touching". At higher densities, the potential function decreases, reaching a minimum at density n_{eq}. For densities higher than n_{eq}, the potential function increases steeply, reaching a maximum at density, $n_{\max}$. In this figure, $n_{min} = 50, n_{eq} = 80$, and $n_{\max} = 100$.
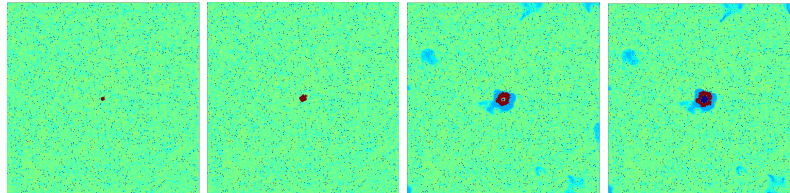

FIGURE 7. Time evolution of a simulation of a slow-growing tumor. From left to right, the panels show tumor growth after 10, 100, 200 and 600 simulated days. Viable tumor cells are colored red, normal cells are yellow and green, and necrotic cells are dark blue. The simulations show that a necrotic core begins to develop by 200 days.
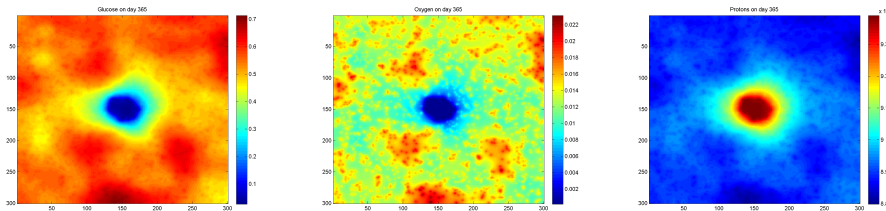

FIGURE 8. Nutrient Concentrations after 365 days. Left: Glucose, Center: Oxygen, Right: H$^+$ ions.
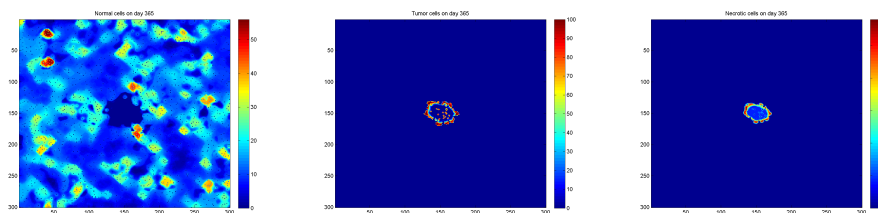
FIGURE 9. Cell Populations: Left: normal cells, Center: tumor cells, Right: necrotic cells.

implemented three pertinent boundary conditions for our biological simulations: *periodic grid topology*, *fixed boundary state*, and *zero-flux boundary*. Diffusion and cell movement for each boundary rule is implemented in a computationally efficient manner, exploiting fast algorithms for matrix multiplication. The details are given in Appendix B.

4. **Results.**

4.1. **Nutrient consumption.** The model parameters describing nutrient consumption and the production of lactate were initially calibrated by checking nutrient consumption rates in a variety of micro-environments to make sure that model predictions were consistent with experimental observation. Figure 10 shows oxygen and glucose consumption rates predicted by the model. In the model, tumor cells and normal cells consume oxygen at the same rate, but this rate does depend on local glucose, oxygen and hydrogen concentrations. Since normal pH levels are around 7.4 [64], it is the top left graph in each set that are the most significant to our current study. The upper set of graphs show glucose consumption rates as a function of oxygen concentration at four different levels of acidity. Consumption rates for tumor cells (solid lines) and normal cells (dashed lines) are drawn on the same axes for comparison. We see that the difference in consumption rates as most marked at pH levels close to normal, and when oxygen concentrations are low. In these graphs, the glucose concentration is fixed at 5.5 mM. The lower set of graphs shows oxygen consumption rates as a function of oxygen concentration at two different glucose concentrations and four different levels of acidity. Here we see that at lower glucose levels oxygen consumption rates are significantly higher than at normal glucose levels, consistent with [14]. As acidity increases, this difference diminishes.

4.2. **Tumor growth and micro-environment.** In this section we describe the results of some experiments with the model. Figure 9 shows the results of a simulation run for 365 days on a 300 by 300 grid with randomly distributed blood vessels beginning with a very small initial tumor population. Normal cell populations, shown on the left, are unaffected away from the tumor. Consistent with diffusion-limited growth, the tumor has developed a necrotic core and a proliferating rim. The center and right panels show that the tumor has become necrotic in the center. Figure 8 shows nutrient concentrations for the same simulations. The left panel shows little glucose diffusing to the interior, and the center panel shows that the center of the tumor has become hypoxic. The right panel shows the effect
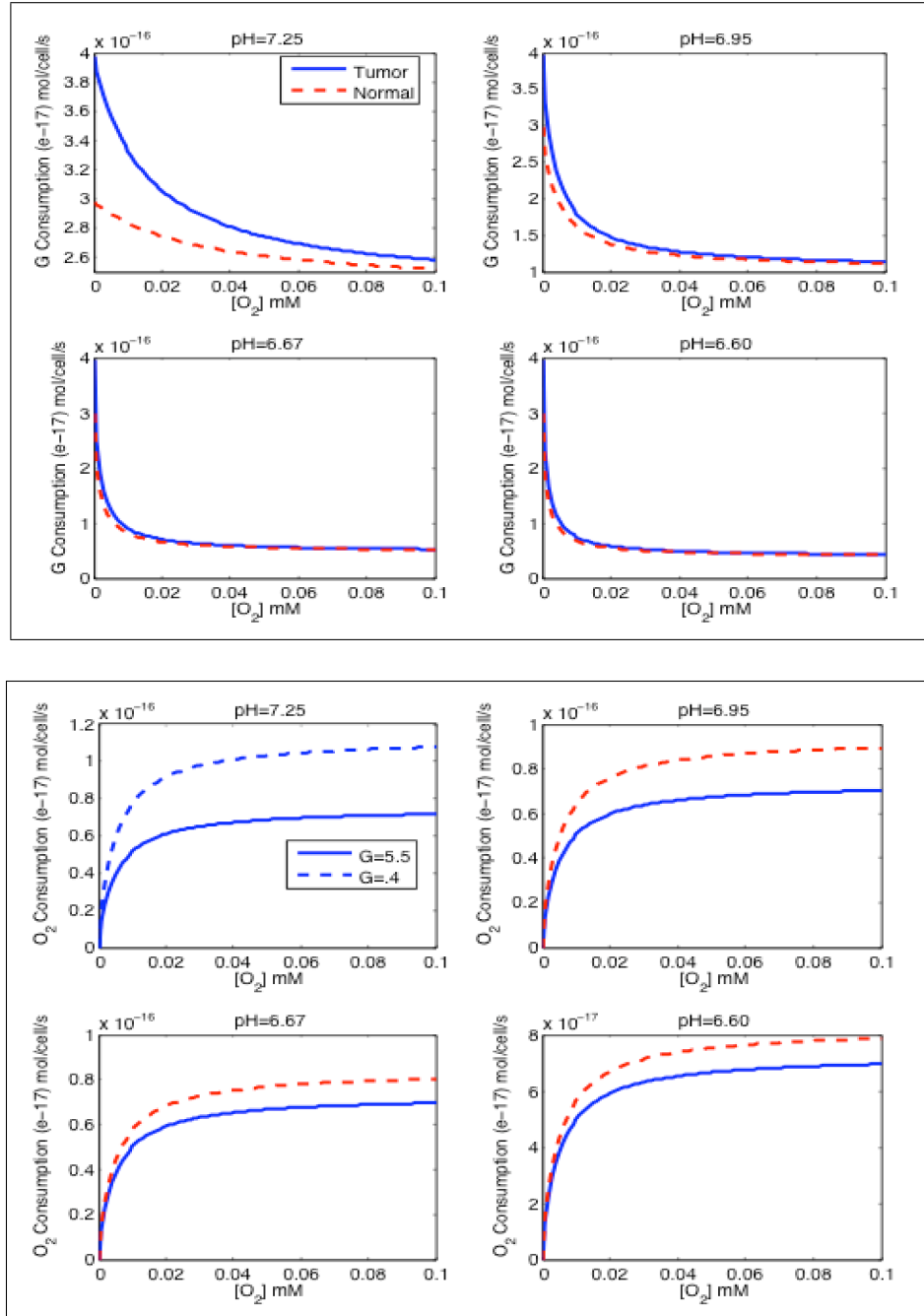
FIGURE 10. Nutrient consumption rates as a function of oxygen concentration. Upper two rows: glucose consumption for tumor (solid lines) and normal (dashed lines) cells at four different pH levels, $[G] = 5.5mM$; lower two rows: oxygen consumption rates at two different glucose levels (solid lines: $[G] = 5mM$, dashed lines: $[G] = .4mM$) and four different pH levels.
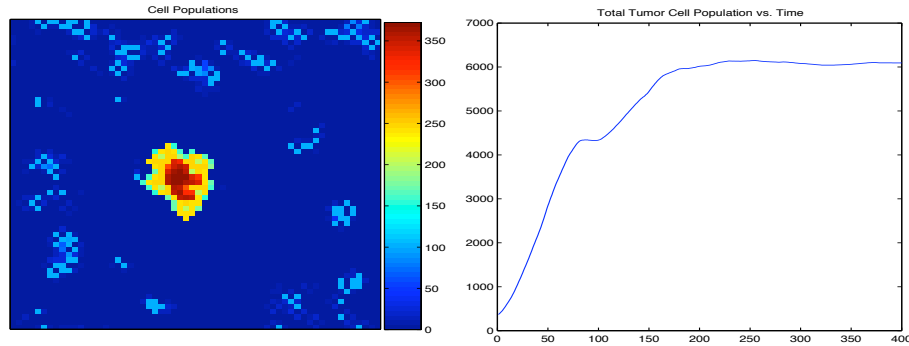
FIGURE 11. Simulation showing the final tumor after 400 days
(left) and total tumor population over time (right). In this case,
tumor growth is diffusion limited, and the tumor will grow no fur-
ther unless new blood vessels are formed.

of the tumor on the acidity of the surrounding tissue: far from the tumor, pH lev-
els approach normal, but nearby and in the center of the tissue, the environment
has become relatively acidic. Figure 11 illustrates that the inability of nutrients
to penetrate the core of the tumor limits its ability to grow beyond a certain size,
measured in terms of total population. In this simulation, adhesion parameters and
the distribution of blood vessels are kept constant. If the tumor cells have the abil-
ity to encourage the growth of new vasculature (angiogenesis) or to reduce cell-cell
adhesion, then the tumor has the ability to grow beyond this limiting population.
These preliminary simulations suggest that the model adequately captures these
features of tumor growth, so that mechanisms involved in the progression of the
disease can then be explored.

All of our results reflect the assumption that tumor cells are able to metabolize
glycolytically more readily than normal cells: glycolysis produces more lactate and
is less efficient than aerobic metabolism, and so the O_2 concentrations and the pH of
the tissue surrounding the tumor is decreased, and the tissue occupied by the tumor
cells becomes hypoxic and more acidic. These changes in the micro-environment
have consequences not only for the normal cells and the overall energy budget of the
host, but can also affect the delivery and bio-distribution of potential treatments,
a factor that we propose to explore with this model. We note that these results are
consistent with observations from both *in vitro* and *in vivo* studies (e.g. [58], [38],
[32]).

4.3. **The effect of glucose levels and adhesivity.** Figure 12 shows that tumor
growth is enhanced by increased glucose levels in the blood vessels. Additionally,
a loss in adhesivity can enable the cells to migrate to more favorable regions of
tissue, thereby escaping the diffusive limit. Figure 13 shows the available ATP at
the end of the same simulations. The white contour, visible in the graph of ATP
levels under "normal" conditions, encloses a cross-sectional area of tumor that is
unable to sustain cell life. The contour is not visible in the other two graphs, since
cells either have more glucose available (middle graph) or are able to migrate more
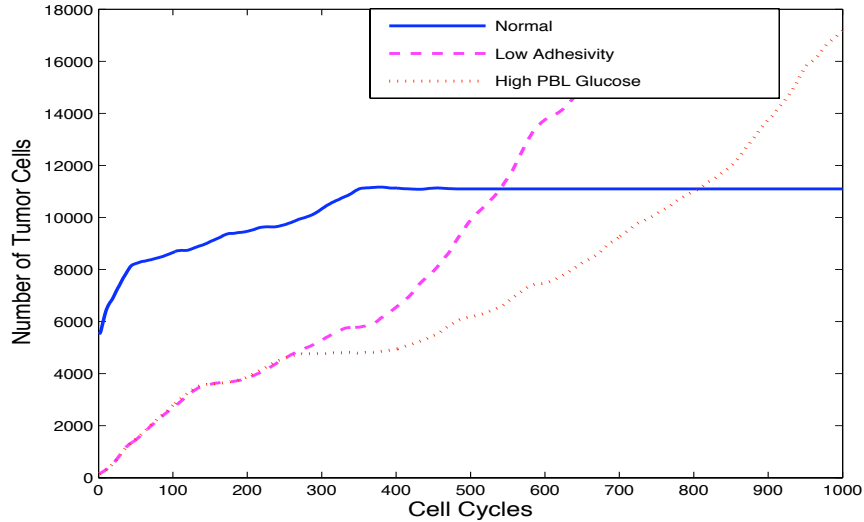freely towards areas of higher nutrient concentration (rightmost graph).

FIGURE 12. Three different simulations illustrating the effect of glucose levels and cell-cell adhesivity. The solid line shows growth with parameter values considered to be in the normal range (solid line), showing that the tumor population reaches a steady state of approximately 11000 cells. A lower adhesivity coefficient ($t_{eq} = 60$ instead of 90) leads to unbounded growth after 1000 days (dashed line), as does an abnormally high peripheral blood level (PBL) of glucose ($G_{bv} = 5.3$ instead of 5.25).
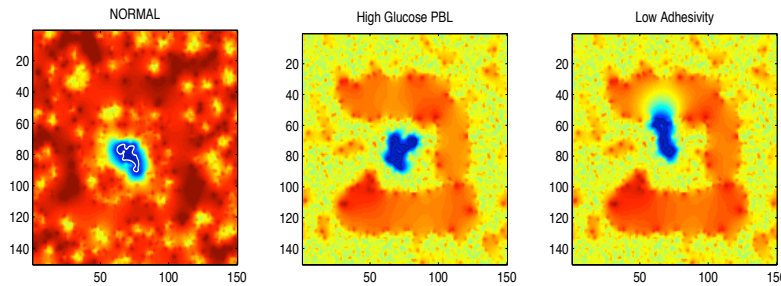

FIGURE 13. Graphs of the available ATP over the simulation grid at the end of the simulations shown in Figure 12. The contour, visible in the leftmost graph, encloses a cross-sectional area that is unable to sustain cell growth.

5. **Discussion and future directions.** We have developed a two-dimensional hybrid cellular automaton model of tumor growth in tissue that incorporates the effects of the cancer cells on the micro-environment. In particular, the model reflects a cancer cell's ability to metabolize glucose anaerobically and to survive in an acidic environment that can be hostile to normal cells. By calculating the energy available to cells locally, the model predicts that tumor cells have the advantage over normal

cells and are able to invade surrounding tissue under certain conditions. The model has the ability to describe the effects of cell-cell adhesion on the invasiveness of the tumor, and it can also describe vascular constriction and collapse due to pressure from the growing tumor.

The goal of the model is to provide a computationally efficient framework for the investigation of the growth of specific tumors in tissue, of the mechanisms underlying cell metastasis, and of the effects of certain cancer treatments, including combination treatments made up of both chemotherapy and immunotherapy. The model is detailed enough to be calibrated to a specific tumor-cell type, once data describing cell metabolism, tissue vascularization, and tissue density is provided. Once the calibration is completed, the effects of certain treatments can be simulated. For example, the administration of a cytotoxic drug can be modeled by adding a state variable describing the delivery and diffusion of the drug through the tissue once the diffusion constant of the drug is known as well as its cytolytic potential. We have developed equations describing fractional cell kill by a chemotherapeutic drug in [19], [20] and [54], while we have modeled immunotherapy and combination therapy in [21], [22] and [17]. The equations describing the effects of the drug on the tumor cells and normal cells, as well as the interactions between immune cells and tumor cells can be used in this CA model by using them as local evolutionary rules. Recruitment and proliferation of immune cells must also be added to the current model. Some of the ideas from the authors' previous work in [18] describing a cellular automaton model can be used, although the probabilistic rules in that earlier model will be translated to deterministic laws, in line with this model's attempt to rely on tissue heterogeneity and the nonlinear nature of the interactions to generate the complicated and unpredictable behavior observed in actual tumor growth.

It is known that oxygen concentrations can be an important factor in the effectiveness of radiotherapy as well as in the progression of the disease by metastasis (e.g. [9], [12]). The model presented here could serve as a refinement of earlier models such as [5] and [50] that investigate the role of oxygen concentrations on radiotherapy and the delivery of chemotherapeutic agents. By appealing to the insights offered in these and other works, we plan to use this DEB-based model to connect the microscopic effects of therapy to overall host fitness.

The simulation could be extended to model tumor development in three-dimensional tissue rather than an effectively two-dimensional tissue slice. This would require several modifications to simulation data structures and an adjustment to the Dirty Diffusion computation. Dirty Diffusion as described in this paper is a matrix multiplication-based operation; since matrix multiplication is defined only for two-dimensional matrices, running a single matrix multiplication as described in §B.0.1 would no longer be possible. Instead, the three dimensional n-by-n-by-n nutrient concentration matrix N would be treated as a stack of n two-dimensional matrices $[N_0, N_1, \ldots, N_{n-1}]$. Dirty diffusion would then be accomplished for each matrix N_x by performing the following computation:

$$N_{x,t+1} = \frac{A \times N_{x,t} + N_{x,t} \times B + N_{x-1,t} + N_{x+1,t}}{6}. \tag{19}$$

Thus, addition of adjacent grid elements within a two-dimensional slice is accomplished using matrix multiplication as before, whereas addition of neighboring elements in adjacent slices is accomplished using matrix addition.

Appendix A. **Parameter values.** Table A lists the parameter values used in the simulations.

Parameter	Description	Value [2]
necPersistence	Fraction of necrotic cells remaining after end of timestep	0.9
nodeVolume	Volume of each grid element	1×10^{-6} mL
nodeLength	Side length of each grid element	$13.23\,\mu$m
maxPop	Maximum cell population in a grid element	100 cells
initNormalPop	Number of normal cells per grid element when starting a new simulation	12 cells
vesselSize	Amount of space (in cells) consumed by each blood vessel	25 cells
t_max	Maximum number of tumor cells per grid element, eq. (10)	100 cells
t_min	Minimum number of tumor cells for adhesion to take effect, eq. (10)	0 cells
dMATPt_dt	ATP needed (per cell) for tumor cells to survive, eq. (18)	3.04×10^{-16} mo/c/s [3]
dMATPn_dt	ATP needed (per cell) for normal cells to survive, eq. (18)	4.48×10^{-16} mo/c/s
dGATPt_dt	ATP needed (per cell) for tumor cells to reproduce, eq. (18)	1.5×10^{-16} mo/c/s
dGATPn_dt	ATP (per cell) needed for normal cells to reproduce, eq. (18)	2×10^{-16} mo/c/s
growth_thresh	Minimum fraction by which cell populations in a grid element can change	0.01
cons_ctumor	c_{tumor}, consumption eq. (13)	2
cons_cnorm	c_{normal}, consumption eq. (13)	1
cons_aO	a_O, consumption eq. (11)	7.2×10^{-17} mo/c/s [4]
cons_bO	b_O, consumption eq. (11)	$2 \times 10^{-21} \dfrac{\text{mo}(\text{mM})^{n+1}}{\text{cs}}$
cons_kO	k_O, consumption eq. (11)	4.6×10^{-3} mM
cons_n	n, exponent in eq. (11)	0.92
cons_aG	a_G, consumption eq. (12)	$1.9 \times 10^{-21} \dfrac{\text{mo}(\text{mM})^{m}}{\text{cs}}$
cons_bG	b_G, consumption eq. (12)	$1.9 \times 10^{-23} \dfrac{\text{mo}(\text{mM})^{m+1}}{\text{cs}}$
cons_kG	k_G, consumption eq. (12)	4×10^{-2} mM
cons_m	m, exponent in eq. (12)	1.2

---

[2]Unitless if no units are noted.

[3]moles ATP/cell/sec

[4]moles per cell per second

|		
`cons_qtumor`	q_{tumor}, consumption eq. (13)	4×10^{-16} mo/c/s
`cons_qnormal`	q_{normal}, consumption eq. (13)	3×10^{-16} mo/c/s
`minConc`	Minimum nutrient concentration to avoid divide-by-zero errors	1×10^{-8} mM
`GThreshold`	Minimum glucose concentration change required to continue simulating diffusion in current timestep	2×10^{-4} mM
`OThreshold`	Minimum oxygen concentration change required to continue simulating diffusion in current timestep	2×10^{-5} mM
`D_G`	Glucose diffusion coefficient	5×10^{-6} cm^2/s
`D_O`	Oxygen diffusion coefficient	1.46×10^{-5} cm^2/s
`D_H`	Proton diffusion coefficient	1.08×10^{-5} cm^2/s
`protonFactor`	Fraction of protons not neutralized by buffers	1×10^{-5}
`lacToGluc`	Ratio of proton production to anaerobic glucose metabolism	1.56
`G_o`	Starting glucose concentration when running a new simulation	3.75 mM
`G_bv`	Glucose concentration in blood	5.25 mM
`G_q`	Controls permeability of glucose through blood vessel walls	$1\,\mu\mathrm{m\,s}^{-1}$
`pH_o`	Starting pH when running a new simulation	7.3
`pH_bv`	Blood pH	7.35
`H_q`	Controls permeability of protons through blood vessel walls	$2.34\,\mu\mathrm{m\,s}^{-1}$
`O_o`	Starting oxygen concentration when running a new simulation	0.26 mM
`O_bv`	Oxygen concentration in blood	0.5 mM
`O_q`	Controls permeability of oxygen through blood vessel walls	$5\,\mu\mathrm{m\,s}^{-1}$
`phosToOxy`	Ratio of phosphorus to oxygen used to compute ATP production	2.36
`atpPerGlucAer`	Molecules of ATP produced through aerobic metabolism of one glucose molecule	30 molecules
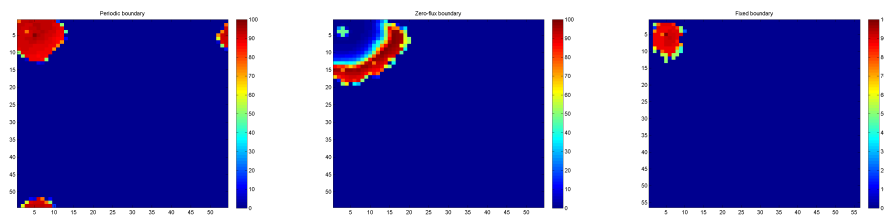
FIGURE 14. A comparison of the three boundary-value rules using the same initial conditions: Periodic (left), Zero Flux (center) and Fixed (right).

atpPerGlucAnaer	Molecules of ATP produced through anaerobic metabolism of one glucose molecule	0.75 molecules
minConcChange	Minimum nutrient concentration change during diffusion	1×10^{-4} mM
secondsPerDay	Number of seconds in 24 hours	86 400 s

Table 1: Baseline parameters used in model simulations.

Appendix B. **Implementation of boundary rules.** We have implemented three different boundary rules, illustrated in Figure 14. In general, simulations with periodic grid topology or zero-flux boundaries demonstrate biologically realistic tumor growth patterns. Simulations with fixed boundary state demonstrate biologically realistic growth only if the boundary's fixed nutrient concentrations are appropriately tuned. The three boundary rules can be implemented in similar ways and have similar computational costs. For completeness, we include here a discussion of the methods used to implement each type of boundary. It is certainly possible to perform simulations where the different boundary rules are combined should that be desirable.

B.0.1. *Periodic Grid Topology.* In simulations with periodic grid topology, edge elements are assumed to be adjacent to the element at the opposite grid boundary; nutrient diffusion and cell movement between "neighboring" elements therefore occur across grid boundaries. Diffusion and cell movement in periodic grids is implemented using multiplication with two specific matrixes, A and B, shown in Figure 15.

Figure 15 illustrates the simulation of one timestep of nutrient diffusion in an n-by-n periodic grid. Grid-wide nutrient concentrations are stored in an n-by-n matrix N, with each entry containing the nutrient concentration in the corresponding grid element. To apply the diffusion rule in equation 8, the matrix multiplication $A \times N$ is carried out; as shown in Figure 15, each entry (r, c) in the resulting matrix selfPlusVertNeighbors contains the sum of the entries (r, c), $((r + 1) \bmod n, c)$, and $((r - 1) \bmod n, c)$, i.e., each entry contains its own nutrient concentration plus that of its vertical neighbors. Values for entries in which $r = 0$, the top row, are added to values in the second row and the bottom row; this multiplication therefore enforces vertical periodic grid topology.

$$
\overset{A}{\begin{bmatrix} 1 & 1 & 0 & 1 \\ 1 & 1 & 1 & 0 \\ 0 & 1 & 1 & 1 \\ 1 & 0 & 1 & 1 \end{bmatrix}} \times \overset{N}{\begin{bmatrix} a & b & c & d \\ e & f & g & h \\ i & j & k & l \\ m & n & o & p \end{bmatrix}} =
$$

$$
\begin{bmatrix} a+e+m & b+f+n & c+g+o & d+h+p \\ e+i+a & f+j+n & g+k+c & h+l+d \\ e+i+m & f+j+n & g+k+o & h+l+p \\ a+i+m & b+j+n & c+k+o & d+l+p \end{bmatrix} = selfPlusVertNeighbors
$$

$$
\overset{N}{\begin{bmatrix} a & b & c & d \\ e & f & g & h \\ i & j & k & l \\ m & n & o & p \end{bmatrix}} \times \overset{B}{\begin{bmatrix} 0 & 1 & 0 & 1 \\ 1 & 0 & 1 & 0 \\ 0 & 1 & 0 & 1 \\ 1 & 0 & 1 & 0 \end{bmatrix}} =
$$

$$
\begin{bmatrix} b+d & a+c & b+d & a+c \\ f+h & e+g & f+h & e+g \\ j+l & i+k & j+l & i+k \\ n+p & m+o & n+p & m+o \end{bmatrix} = horizontalNeighbors
$$

FIGURE 15. Implementation of periodic grid topology. N is a cellular automaton grid containing nutrient concentrations. The matrix multiplication $A \times N$ yields the matrix *selfPlusVertNeighbors*. The multiplication $N \times B$ yields *horizontalNeighbors*. These two matrices are then added, and the resulting matrix is divided by 5 to complete the diffusion calculation.

Similarly, the matrix multiplication $N \times B$ is then calculated to produce matrix `horizontalNeighbors`, which contains the sum of each grid element's horizontal neighbors while enforcing horizontal periodic grid topology. The two product matrices are then added, and their results are divided by 5 to produce the final result, in which each element contains the average nutrient concentration of it and its four adjacent elements, with element adjacency defined using periodic grid topology. The calculation of nutrient diffusion with periodic topology is summarized in equation 20:

$$
N_{t+1} = \frac{A \times N_t + N_t \times B}{5} \tag{20}
$$

Where N_t is the matrix of gridwide nutrient concentrations at timestep t.

B.0.2. *Fixed Boundary State.* The implementation of fixed boundary state is based on that of periodic grid topology. To simulate diffusion with fixed boundary state on an n-by-n grid, a list `edgeVals` of n precomputed nutrient concetrations is stored; this list specifies the fixed state of the grid boundary. equation 20 is then used to calculate matrix N_{t+1} from N_t as if the grid had periodic topology. The resulting matrix N_{t+1} has invalid values in all edge elements, because the grid boundary state should be fixed; however, all other elements have valid nutrient concentrations. Finally, list `edgeVals` is copied into each of the four grid edges, restoring the fixed boundary state and completing the diffusion calculation.

FIGURE 16. Illustration of the values in the *numNeigh* matrix used to implement zero-flux boundary conditions. Lower case letters show the neighbors of the cell with the corresponding upper case letter.

In order to produce a biologically realistic simulation, `edgeVals` must be accurately tuned. If the nutrient concentrations in `edgeVals` are high, the simulated tumor will grow outward toward the grid edges, which contain a plentiful, inexhaustible supply of nutrients. If the nutrient concentrations in `edgeVals` are low, grid-wide nutrient concentration levels may decrease below the threshold required for tumor survival.

Values in list `edgeVals` were set for an n-by-n grid using the following procedure. A tumor-free simulation was run on an n-by-n grid G with zero-flux boundaries for 500 timesteps, in order to allow grid-wide nutrient concentrations to reach a steady state in the absence of tumor cells. The nutrient concentrations in the edges of G were then used as the values for `edgeVals` in an n-by-n tumor simulation with fixed boundary state.

B.0.3. *Zero-Flux Boundary.* In simulations with a zero-flux boundary, grid elements do not all have the same number of neighbors — edge and corner elements have fewer neighbors than central elements. Thus, the denominator of the diffusion rule in equation 8 is no longer the constant value 5; it is replaced by a value from the matrix `numNeigh`, illustrated in Figure 16:

$$N_{t+1}(r,c) = \frac{N_t(r,c) + \sum_{(i,j)\in\text{nbhd}(r,c)} N_t(i,j)}{\texttt{numNeigh}(r,c) + 1} \tag{21}$$

Where $N_t(r.c)$ is the nutrient concentration in element (r,c) at time t, $\texttt{numNeigh}(r,c)$ is element (r,c) of the `numNeigh` matrix, and $\text{nbhd}(r,c)$ is the set of all elements (i,j) that are adjacent to element (r,c). For example, $\text{nbhd}(0,0) = \{(1,0),(0,1)\}$.

Because each element $N_{t+1}(i,j)$ receives the average concentration in $N_t(i,j)$ and $\text{nbhd}(i,j)$, the denominator in equation 21 must be equal to $|\text{nbhd}(i,j)| + 1$. With periodic grid topology, $|\text{nbhd}(i,j)| = 4$ for all grid elements; however, $|\text{nbhd}(i,j)|$ varies with location in a grid with zero-flux boundaries, requiring the use of `numNeigh`. Matrix multiplication is used to calculate total neighborhood nutrient concentrations with zero-flux boundaries by using the matrices A' and B', as shown in Figure 17.

B.0.4. *Alternative Implementation.* The previous sections describe an implementation of the three boundary rules based on matrix multiplication. Alternatively, a looping-based approach can be used, in which Equations (8) or (21) are directly applied to individual elements. This approach requires a separate computation for each grid element, so its computational complexity is in $O(n^2)$ on an n-by-n grid.

$$
\begin{array}{cc}
A' & N
\end{array}
$$

$$
\begin{bmatrix}
1 & 1 & 0 & 0 \\
1 & 1 & 1 & 0 \\
0 & 1 & 1 & 1 \\
0 & 0 & 1 & 1
\end{bmatrix}
\times
\begin{bmatrix}
a & b & c & d \\
e & f & g & h \\
i & j & k & l \\
m & n & o & p
\end{bmatrix}
=
$$

$$
\begin{bmatrix}
a+e & b+f & c+g & d+h \\
e+i+a & f+j+n & g+k+c & h+l+d \\
e+i+m & f+j+n & g+k+o & h+l+p \\
i+m & j+n & k+o & l+p
\end{bmatrix}
= selfPlusVertNeighbors
$$

$$
\begin{array}{cc}
N & B'
\end{array}
$$

$$
\begin{bmatrix}
a & b & c & d \\
e & f & g & h \\
i & j & k & l \\
m & n & o & p
\end{bmatrix}
\times
\begin{bmatrix}
0 & 1 & 0 & 0 \\
1 & 0 & 1 & 0 \\
0 & 1 & 0 & 1 \\
0 & 0 & 1 & 0
\end{bmatrix}
=
$$

$$
\begin{bmatrix}
b & a+c & b+d & c \\
f & e+g & f+h & g \\
j & i+k & j+l & k \\
n & m+o & n+p & o
\end{bmatrix}
= horizontalNeighbors
$$

FIGURE 17. Implementation of zero-flux boundaries. N is a cellular automaton grid containing nutrient concentrations. The matrix multiplication $A' \times N$ yields the matrix *selfPlusVertNeighbors*. The multiplication $N \times B'$ yields *horizontalNeighbors*. These two matrices are then added, and the resulting matrix element-wise divided by matrix `numNeigh` to complete the diffusion calculation.

In contrast, the computational complexity of the matrix multiplication-based approach is in $O(n^3)$; however, in practice, the matrix multiplication-based method performs much faster than the looping-based method.

REFERENCES

[1] T. Alarcón, H. M. Byrne and P. K. Maini, *A cellular automaton model for tumour growth in inhomogeneous environment*, Journal of Theoretical Biology, **225** (2003), 257–274.

[2] A. Alt-Holland, W. Zhang, A. Margulis and J. Garlick, *Microenvironmental control of pre-malignant disease: the role of intercellular adhesion in the progression of squamous cell carcinoma*, Seminars in Cancer Biology, **15** (2005), 84–96.

[3] A. R. A. Anderson and M. A. J. Chaplain, *Continuous and discrete mathematical models of tumor-induced angiogenesis*, Bulletin of Mathematical Biology, **60** (1998), 857–900.

[4] M. Bernaschi and F. Castiglione, *Design and implementation of an immune system simulator*, Computers in Biology and Medicine, **31** (2001), 303–331.

[5] A. Bertuzzi, A. d'Onofrio, A. Fasano and A. Gandolfi, *Regression and regrowth of tumor cords following single dose anticancer treatment*, Bulletin of Mathematical Biology, **65** (2003), 903–931.

[6] A. Bertuzzi, A. Fasano, A. Gandolfi and C. Sinisgalli, *ATP production and necrosis formation in a tumour spheroid model*, Mathematical Modelling of Natural Phenomena, **2** (2007), 30–46.

[7] A. Bertuzzi, A. Fasano, A. Gandolfi and C. Sinisgalli, *Necrotic core in EMT6/Ro tumour spheroids: Is it caused by an ATP deficit?*, Journal of Theoretical Biology, **262** (2010), 142–150.

[8] B. Blouw, H. Song, T. Tihan, J. Bosze, N. Ferrara, H. Gerber, R. Johnson and G. Bergers, *The hypoxic response of tumors is dependent on their microenvironment*, Cancer Cell, **4** (2003), 133–146.

[9] R. Bristow and R. Hill, *Molecular and cellular basis of radiotherapy*, in "The Basic Science of Oncology" (editors, I. Tannock and R. Hill), 295–321. McGraw Hill, New York, (1998).

[10] H. Byrne and M. Chaplain, *Modelling the role of cell-cell adhesion in the growth and development of carcinomas*, Mathematical and Computational Modelling, **24** (1996), 1–17.

[11] H. Byrne and M. Chaplain, *Free boundary value problems associated with the growth and development of multicellular spheroids*, European Journal of Applied Mathematics, **8** (1997), 639–658.

[12] R. Cairns and R. Hill, *Acute hypoxia enhances spontaneous lymph node metastasis in an orthotopic murine model of human cervical carcinoma*, Cancer Research, **64** March (2004), 2054–2061.

[13] J. Casciari and J. Rasey, *Determination of the radiobiologically hypoxic fraction in multicellular spheroids from data on the uptake of [3H]fluoromisonidazole*, Radiat Res., **141** (1995), 28–36.

[14] J. Casciari, S. Sotirchos and R. Sutherland, *Variations in tumor cell growth rates and metabolism with oxygen concentration, glucose concentration, and extracellular pH*, Journal of Cellular Physiology, **151** (1992), 386–394.

[15] M. Chaplain and A. Matzavinos, *Mathematical modelling of spatio-temporal phenomena in tumour immunology*, Lect. Notes Math., **1872** (2006), 131–183.

[16] V. Cristini, J. Lowengrub and Q. Nie, *Nonlinear simulation of tumor growth*, J Math Biol., **46** (2003), 191–224.

[17] L. de Pillis, W. Gu and A. Radunskaya, *Mixed immunotherapy and chemotherapy of tumors: Modeling applications and biological interpretations*, Journal of Theoretical Biology, **238** September (2005), 841–862.

[18] L. de Pillis, D. Mallet and A. Radunskaya, *Spatial tumor-immune modeling*, Journal of Computational and Mathematical Models in Medicine, **7** June-September (2006), 159–276.

[19] L. de Pillis and A. Radunskaya, *A mathematical tumor model with immune resistance and drug therapy: An optimal control approach*, J Theor Med., **3** (2001), 79–100.

[20] L. de Pillis and A. Radunskaya, *The dynamics of an optimally controlled tumor model: A case study*, Math Comput Model. (Special Issues), **37** (2003), 1221–1244.

[21] L. de Pillis and A. Radunskaya, *Immune response to tumor invasion*, in "Computational Fluid and Solid Mechanics" (editor, K. Bathe), M.I.T., **2** (2003), 1661–1668.

[22] L. de Pillis, A. Radunskaya and C. Wiseman, *A validated mathematical model of cell-mediated immune response to tumor growth*, Cancer Research, **65** September (2005), 7950–7958.

[23] M. Dewhirst, *Concepts of oxygen transport at the microcirculatory level*, Semin Radiat Oncol., **8** (1998), 143–50.

[24] S. Dormann and A. Deutsch, *Modeling of self-organized avascular tumor growth with a hybrid cellular automaton*, In Silico Biology, **2** (2002), 0035.

[25] A. dos Reis, J. Mombach, M. Walter and de Avila L. F., *The interplay between cell adhesion and environment rigidity in the morphology of tumors*, Phyisca A-Statistical Mechanics and its Applications, **322** (2003), 546–554.

[26] R. D'Souza, N. Margolus and M. Smith, *Dimension-splitting for simplifying diffusion in lattice-gas models*, Journal of Statistical Physics, **107** (2002).

[27] S. C. Ferreira, M. L. Martins and M. J. Vilela, *Reaction-diffusion model for the growth of avascular tumor*, Phys Rev E, **65** (2002).

[28] P. Gassmann, J. Haier and G. Nicolson, *Cell adhesion and invasion during secondary tumor formation*, Cancer Growth and Progression, **3** (2004).

[29] R. Gatenby and J. Gillies, *Why do cancers have high aerobic glycolysis?*, Nature Reviews Cancer, **4** (2004), 891–899.

[30] I. Georgoudas, G. Sirakoulis and I. Andreadis, *An intelligent cellular automaton model for crowd evacuation in fire spreading conditions*, in "19th IEEE International Conference on Tools with Artificial Intelligence (ICTAI 2007)" **1** 36–43. IEEE Computer Society, (2007).

[31] S. Gobron and N. Chiba, *Visual simulation of crack pattern based on 3D surface cellular automaton*, in "Seventh International Conference on Parallel and Distributed Systems Workshops (ICPADS'00 Workshops)", pages 181–187. IEEE Computer Society, (2000).

[32] M. Gryczynskia, J. Kobos and W. Pietruszewska, *Intratumoral microvessels density and morphometric study of angiogenesis as prognostic factor in laryngeal cancer*, International Congress Series, **1240** (2003), 1113–1118.

[33] M. Guppy, P. Leedman, X. Zu and V. Russel, *Contribution by different fuels and metabolic pathways to the total ATP turnover of proliferating MCF-7 breast cancer cells*, Biochem. J., **364** (2002), 309–315.

[34] J. Haier and G. Nicolson, *Role of tumor cell adhesion as an important factor in formation of distant metastases*, Diseases Colon Rect., **44** (2001), 876–884.

[35] A. Harris, "Hypoxia - A Key Regulatory Factor in Tumour Growth," 2002.

[36] G. Helmlinger, A. Sckell, M. Dellian, N. Forbes and R. Jain, *Acid production in glycolysis-impaired tumors provides new insights into tumor metabolism*, Clinical Cancer Research, **8** (2002), 1284–1291.

[37] M. Hockel and P. Vaupel, "Tumor Hypoxia: Definitions and Current Clinical, Biologic, and Molecular Aspects," 2001.

[38] M. Hystad and E. Rofstad, *Oxygen consumption rate and mitochondrial density in human melanoma monolayer cultures and multicellular spheroids*, Int J Cancer., **57** (1994), 532–537.

[39] T. L. Jackson, *Vascular tumor growth and treatment: Consequenes of polyclonality, competition and dynamic vascular support*, J Math Biol., **44** Mar.(2002), 201–226.

[40] S. Kooijman, "Dynamic Energy and Mass Budgets in Biological Systems," Cambridge University Press, Great Britain, 2nd edition, 2000.

[41] M. I. Koukourakis, M. Pitiakoudis, A. Giatromanolaki, A. Tsarouha, A. Polychronidis, E. Sivridis and C. Simopoulos, *Oxygen and glucose consumption in gastrointestinal adenocarcinomas: Correlation with markers of hypoxia, acidity and anaerobic glycolysis*, Cancer Science, **97** (2006), 1056–1060.

[42] M. Kunz, S. Moeller, D. Koczan, P. Lorenz, R. Wenger, M. Glocker, H. Thiesen, G. Gross and S. Ibrahim, *Mechanisms of hypoxic gene regulation of angiogenesis factor Cyr61 in melanoma cells*, Journal of Biological Chemistry, **278** (2003), 45651–45660.

[43] M. Li, Z. Ru and J. He, *Cellular automata to simulate rock failure*, in "16th International Conference on Artificial Reality and Telexistence–Workshops (ICAT'06)", 110–114. IEEE Computer Society, (2006).

[44] P. Macklin, S. McDougall, A. Anderson, M. Chaplain, V. Cristini and J. Lowengrub, *Multiscale modelling and nonlinear simulation of vascular tumour growth*, Journal of Mathematical Biology, **58** (2009), 765–798.

[45] D. Mallet and L. de Pillis, *A cellular automata model of tumor-immune system interactions*, Journal of Theoretical Biology, **239** (2006), 334–350.

[46] C. Menon, G. Polin, I. Prabakaran, A. Hsi, C. Cheung, J. Culver, J. Pingpank, C. Sehgal, A. Yodh, D. Buerk and D. Fraker, *An integrated approach to measuring tumor oxygen status using human melanoma xenografts as a model*, Cancer Research, **63** (2003), 7232–7240.

[47] B. Mueller, R. Reisfeld, T. Edgington and W. Ruf, *Expression of tissue factor by melanoma cells promotes efficient hematogenous metastasis*, Proc. Natl. Acad. Sci. USA, **89** December (1992), 11832–11836.

[48] D. Nelson and M. Cox, "Lehninger Principles of Biochemistry," W. H. Freeman and Co., 4th edition, 2004.

[49] N. Oriuchi, T. Higuchi, T. Ishikita, M. Miyakubo, H. Hanaoka, Y. Iida and K. Endo, *Present role and future prospects of positron emission tomography in clinical oncology*, Cancer Science, Epub ahead of print, October 2006.

[50] M. Owen, H. Byrne and C. Lewis, *Mathematical modelling of the use of macrophages as vehicles for drug delivery to hypoxic tumour sites*, Journal of Theoretical Biology, **226** (2004), 377–399.

[51] A. Patel, E. Gawlinski, S. Lemieux and R. Gatenby, *A cellular automaton model of early tumor growth and invasion: The effects of native tissue vascularity and increased anaerobic tumor metabolism*, Journal of Theoretical Biology, **213** (2001), 315–331.

[52] L. Preziosi, "Cancer Modelling and Simulation," Mathematical Biology and Medicine Series. Chapman & Hall/CRC, 2003.

[53] R. Puzone, B. Kohler, P. Seiden and F. Celada, *IMMSIM, a flexible model for in machina experiments on immune system responses*, Future Generation Computer Systems, **18** (2002), 961–972.

[54] A. Radunskaya and M. Villasana, *A delay differential equation model for tumor growth*, J. Math.Biol., **47** (2003), 270–294.

[55] K. A. Rejniak, *An immersed boundary framework for modelling the growth of individual cells: An application to the early tumour development*, Journal of Theoretical Biology, **247** JUL 7 (2007), 186–204.

[56] K. A. Rejniak and A. R. A. Anderson, *Hybrid models of tumor growth*, Wiley Interdisciplinary Reviews - Systems Biology and Medicine, **3** Jan-Feb (2011), 115–125.

[57] K. A. Rejniak and L. J. McCawley, *Current trends in mathematical modeling of tumor-microenvironment interactions: a survey of tools and applications*, Experimental Biology and Medicine, **235** April (2010), 411–423.

[58] E. Rofstad and K. Maseide, *Radiobiological and immunohistochemical assessment of hypoxia in human melanoma xenografts: acute and chronic hypoxia in individual tumours*, Int J Radiat Biol., **75** (1999), 1377–93.

[59] S. Sanga, H. B. Frieboes, X. Zheng, R. Gatenby, E. L. Bearer and V. Cristini, *Predictive oncology: A review of multidisciplinary, multiscale in silico modeling linking phenotype, morphology and growth*, NeuroImage, **37** (Supplement 1) (2007), S120 – S134. Proceedings of the International Brain Mapping & Intraoperative Surgical Planning Society Annual Meeting, (2006).

[60] P. Schornack and R. Gillies, *Contributions of cell metabolism and H^+ diffusion to the acidic pH of tumors*, Neoplasia, **5** (2003), 135–145.

[61] T. J. Schulz, R. Thierbach, A. Voigt, G. Drewes, B. Mietzner, P. Steinberg, A. F. H. Pfeiffer and M. Ristow, *Induction of oxidative metabolism by mitochondrial frataxin inhibits cancer growth: Otto warburg revisited*, J. Biol. Chem., **281** (2006), 977–981.

[62] R. Skoyum, K. Eide, K. Berg and E. Rofstad, *Energy metabolism in human melanoma cells under hypoxic and acidic conditions in vitro*, Br J Cancer, **76** (1997), 421–428.

[63] K. Smallbone, R. A. Gatenby, R. Gillies, P. K. Maini and D. Gavaghan, *Metabolic changes during carcinogenesis: Potential impact on invasiveness*, Journal of Theoretical Biology, **244** (2006), 703–713.

[64] K. Smallbone, D. J. Gavaghan, R. A. Gatenby and P. K. Maini, *The role of acidity in solid tumour growth and invasion*, Journal of Theoretical Biology, **234** (2005), 476–484.

[65] J. Smolle, *Cellular automaton simulation of tumour growth – equivocal relationships between simulation parameters and morphologic pattern features*, Anal Cell Pathol., **17** (1998), 71–82.

[66] J. Smolle, R. Hofmann-Wellenhof and H. Kerl, *Pattern interpretation by cellular automata (pica)–evaluation of tumour cell adhesion in human melanomas*, Anal Cell Pathol., **7** (1994), 91–106.

[67] P. Subarsky and R. Hill, *The hypoxic tumour microenvironment and metastatic progression*, Clinical & Experimental Metastasis, **20** (2003), 237–250.

[68] I. Tufto, H. Lyng and E. K. Forstad, *Vascular density in human melanoma xenografts: Relationship to angiogenesis, perfusion and necrosis*, Cancer Letters, **123** (1998), 159–165.

[69] S. Turner, *Using cell potential energy to model the dynamics of adhesive biological cells*, Physical Review E, **71** (2005), pp.12. 041903.

[70] S. Turner, J. Sherratt, K. Painter and N. Savill, *From a discrete to a continuous model of biological cell movement*, Physical Review E, **69** (2004), 021910.

[71] I. van Leeuwen, C. Zonneveld and S. Kooijman, *The embedded tumour: Host physiology is important for the evaluation of tumour growth*, British Journal of Cancer, **89** (2003), 2254–2263.

[72] P. Vaupel, O. Thews, D. Kelleher and M. Hoeckel, *Current status of knowledge and critical issues in tumor oxygenation. results from 25 years research in tumor pathophysiology*, Adv Exp Med Biol., **454** (1998), 591–602.

[73] R. Venkatasubramanian, M. A. Henson and N. S. Forbes, *Incorporating energy metabolism into a growth model of multicellular tumor spheroids*, Journal of Theoretical Biology, **242** (2006), 440–453.

[74] J. von Neumann, "Theory of Self-Reproducing Automata," University of Illinois Press, 1966.

[75] S. Wise, J. Lowengrubb and V. Cristini, *An adaptive multigrid algorithm for simulating solid tumor growth using mixture models*, Mathematical and Computer Modelling, **53** January (2011), 1–20.

[76] X. Zu and M. Guppy, *Cancer metabolism: Facts, fantasy, and fiction*, Biochemical and Biophysical Research Communications, **313** (2004), 459–465.

E-mail address: duboisc@ics.uci.edu
E-mail address: jjfarnha@princeton.edu
E-mail address: eaaron@wesleyan.edu
E-mail address: aradunskaya@pomona.edu